JOURNAL OF GEOPHYSICAL RESEARCH, VOL. 114, D17206, doi:10.1029/2008JD011680, 2009

Multiresolution analysis of the temporal variance and correlation of transmittance and reflectance of an atmospheric column

H. M. Deneke,[1,2] W. H. Knap,[1] and C. Simmer[2]

Received 27 December 2008; revised 29 April 2009; accepted 9 June 2009; published 10 September 2009.

[1] Collocated time series of narrowband 0.6 μm atmospheric flux transmittance at the surface and bidirectional reflectance at the top of atmosphere are decomposed into distinct frequency bands, so as to investigate the timescale dependences of their variance and correlation. Toward this goal, a multiresolution analysis based on the maximum overlap discrete wavelet transform and the Haar wavelet is applied to 5-minute resolution measurements from two multifilter rotating shadowband radiometers operated at Cabauw, NL, and Heselbach, DE, and to observations of the geostationary METEOSAT8 SEVIRI satellite imager. Both time series are best correlated when the satellite data are shifted by about 1 pixel (6 km) to the North, which is likely attributable to the parallax effect caused by the height of cloud tops and the oblique satellite viewing angle. While variations in transmittance and reflectance with periods longer than an hour are found to be highly anticorrelated, the correlation breaks down for shorter periods. Below 1 hour, the transmittance time series also exhibits significantly higher variance than the reflectance. The larger extent of the satellite pixel (6×3 km^2) versus the point nature of the ground measurements is proposed as an explanation. Due to the small contributions of high-frequency variability to the total variance of the reflectance, aliasing effects caused by the 5-minute repeat cycle of SEVIRI are expected to be small. Implications of our findings are discussed for the validation of satellite estimates of solar surface irradiance. Averaging of surface measurements over at least 40 minutes is recommended for a comparison.

Citation: Deneke, H. M., W. H. Knap, and C. Simmer (2009), Multiresolution analysis of the temporal variance and correlation of transmittance and reflectance of an atmospheric column, *J. Geophys. Res.*, *114*, D17206, doi:10.1029/2008JD011680.

1. Introduction

[2] Clouds strongly modulate the earth's radiation budget through their interaction with solar and terrestrial radiation [*Kiehl and Trenberth*, 1997]. Their highly transient nature causes large uncertainties for the interpretation of cloud measurements, and the determination of cloud properties [*Rossow et al.*, 2002; *Stephens and Kummerow*, 2007], and impedes our understanding of cloud processes and cloud-radiation interactions, including their representation in atmospheric models [*Intergovernmental Panel on Climate Change*, 2007].

[3] Current operational cloud property retrievals from meteorological satellite imagers are based on one-dimensional radiative transfer theory. Within this conceptual framework, the reflectance and transmittance of solar radiation at the top and bottom of a cloudy atmospheric column are connected and uniquely determined by the optical properties of the constituents within this column [e.g., *King*, 1987].

[4] In reality, this coupling is only expected to hold for cases resembling the underlying model assumption of a plane-parallel horizontally homogeneous cloud. For clouds with significant small scale variability, horizontal photon transport and radiative smoothing lead to a decorrelation of the variations in reflectance and transmittance [*Barker and Li*, 1997].

[5] Researchers who evaluate satellite products with surface measurements are affected by this issue, as a comparison implicitly assumes that the scaling properties of surface and satellite observations are similar [*Feijt and Jonker*, 2000]. Complications arise from the point nature of surface measurements: variations at spatial scales significantly smaller than the typical pixel size of satellite imagers are resolved [*Schutgens and Roebeling*, 2009; *Greuell and Roebeling*, 2009]. This introduces sampling uncertainties because surface measurements are assumed to be representative for the area of a satellite pixel [*Barker and Li*, 1997]. Prior to a comparison of satellite and surface measurements, suitable temporal and spatial averaging scales must be determined which minimize the impact of these effects on validation statistics.

[6] The goal of this paper is to investigate the impact of temporal averaging on the validation of satellite estimates of solar surface irradiance by a comparison with surface measurements. As temporal variations in the radiance field are mainly induced by clouds, the impact of the length of averaging period will be determined by cloud type [*Duchon and*

[1]Department of Climate Research and Seismology, Royal Netherlands Meteorological Institute, De Bilt, Netherlands.
[2]Meteorological Institute, University of Bonn, Bonn, Germany.

0148-0227/09/2008JD011680$09.00

O'Malley, 1999]. Specifically, the choices made by *Deneke et al.* [2005, 2008] are revisited. However, the results reported are also relevant for other validation studies of satellite-inferred solar surface irradiance.

[7] For this study, the bivariate time series of narrowband 0.6 μm bidirectional reflectance and hemispheric flux transmittance as measured by the METEOSAT SEVIRI instrument and two multifilter rotating shadow-band radiometers operated at Cabauw, the Netherlands, and Heselbach, Germany, are analyzed. As argued by *Nunez et al.* [2005], the 0.6 μm spectral region allows us to study the influence of clouds on solar radiation under idealized conditions, and avoids the complications introduced by aerosol scattering and gaseous absorption in the broadband solar spectral region. Thus our approach avoids assumptions about these constituents which will introduce uncertainties in an actual satellite retrieval.

[8] The multiscale analysis of variance and covariance between two time series based on the maximum overlap discrete wavelet transform is used, which has been introduced by *Percival* [1995] and *Whitcher et al.* [2000]. They have presented wavelet-based estimators of the variance, covariance and cross correlation, and have shown that these quantities decompose the scale-independent estimates for stationary and certain nonstationary time series on a scale-by-scale basis.

[9] The outline of this paper is as follows: in section 2, the two measurement data sets are described. A brief summary of the multiresolution analysis is given in section 3, while a more thorough and mathematical description can be found in the Appendix A. Section 4 investigates the effects of collocation on both time series, presents and discusses the results of the multiresolution analysis, and discusses their relevance for validation of satellite-inferred solar surface irradiance. Conclusions and a brief outlook are given in section 5.

2. Instrumental Data

[10] For this study, narrowband atmospheric flux transmittances measured by two multifilter rotating shadowband radiometers (MFRSRs), one operated at Cabauw, the Netherlands, and the other at Heselbach, Germany, are compared to collocated bidirectional reflectances observed by the METEOSAT SEVIRI satellite imager. A brief overview of both instruments is given next.

[11] METEOSAT is a series of European geostationary meteorological satellites operated by EUMETSAT. The METEOSAT8 and METEOSAT9 satellites are based on the METEOSAT Second Generation design, and carry the SEVIRI (Spinning-Enhanced Visible and InfraRed Imager) instrument. It acquires images in 12 spectral channels, and has a nadir spatial resolution of 3×3 km^2 for all channels except its high resolution visible channel. METEOSAT8 operationally provided images of the complete earth disk with a 15 minute repeat cycle since January 2004, and was replaced by METEOSAT9 as operational satellite in April 2007. METEOSAT8 was positioned at 3.4°W above the equator until April 2008, while METEOSAT9 is located at 0°W. METEOSAT8 images are rectified to 0°W prior to dissemination, however. From June until August 2007, the SEVIRI instrument on METEOSAT8 has been operated in rapid scan mode. This mode acquires images from 15 to 69°N with a 5 minutes repeat cycle. These data were obtained through the EUMETCAST service.

[12] The MFRSRs are of type MFR-7 built by Yankee Environmental Systems, Inc., and measure irradiances for the total solar spectrum and six narrow spectral bands, with widths of about 10 nm. A rotating band periodically shades the direct solar beam, and allows for a separate determination of diffuse and global irradiance. Spectral irradiances are measured using a photodetector together with interference filters. A detailed description of the instrumental design is given by *Harrison et al.* [1994]. Both instruments have recorded data at a 20 second sampling period. These time series have been averaged to 5 minute means centered on the time of the SEVIRI scan for the ground stations. The MFRSR at Heselbach has been deployed as part of the ARM Mobile Facility from March until December 2007 in support of the Convective and Orographically Induced Precipitation Study (COPS [*Wulfmeyer et al.*, 2008]), while the other MFRSR belongs to the permanent instrumentation at the Cabauw meteorological observatory, which is a participant in the baseline surface radiation network (BSRN [*Knap et al.*, 2007]).

[13] Unfortunately, the Cabauw instrument was struck by lightning and failed on the 4 July 2007. Thus measurements from the 1 June, when METEOSAT8 commenced operation in rapid scan mode, until the 4 July have been analyzed for Cabauw, while data until the end of July 2007 are used from Heselbach. All simultaneous SEVIRI and MFRSR observations available from our archive are used in this study. Observations have been limited to values of the cosine of the solar zenith angle larger than 0.1 (about 6° above the horizon), in order to avoid a too low signal-to-noise ratio, sphericity effects on radiative transfer, and uncertainties related to the long optical path through the atmosphere. No other selection criteria have been used. The geographic coordinates of the stations, the corresponding pixel indices within the SEVIRI images, the length of the measurement period, and the unique number of days included in this study during June and July 2007 are given in Table 1. In addition, the pixel indices leading to the best match between satellite and ground time series are listed (see section 4.1 for details).

[14] The Cabauw site is located in the western part of the Netherlands at a distance of about 55 km from the North Sea and 0.7 m below sea level. Its surrounding is typical for this region, with pastures, agricultural areas, only few settlements and negligible elevation changes in its vicinity. In contrast, the Heselbach site is situated in the Murg Valley in the Northern part of the Black Forest at an elevation of 511 m above sea level, and about 30 km to the East of the Rhine Valley. Due to predominantly westerly atmospheric flows, combined with the pronounced orography of the Black Forest mountain range, this region is characterized by extensive convective activity and frequent thunderstorms in summer. At both sites, precipitation during the study period significantly exceeded climatological averages, while temperatures were just slightly above average. Clouds and precipitation were predominantly of convective nature, with several strong showers and thunderstorms. Nevertheless, also a small number of stratiform rain events due to frontal passages over both sites occurred during the study period.

Table 1. Station Names, Geographic Coordinates, Pixel Indices Within the SEVIRI Image for the Stations, the Pixels With the Highest Explained Variance Between Satellite and Ground Observation, and the Measurement Period and Unique Number of Days for Which Collocated SEVIRI and Multifilter Rotating Shadowband Radiometer Observations are Available for June and July 2007

Station	Location	Pixel Station	Best Pixel	Data June	Data July
Cabauw	51.97°N, 4.94°E	1750.5x, 3407.0y	1751x, 3408y	283.3 h/23 days	51.3 h/4 days
Heselbach	48.54°N, 8.40°E	1661.9x, 3342.1y	1662x, 3343y	317.4 h/26 days	390.2 h/30 days

[15] We compare data from the 635 nm and the 670 nm channels from SEVIRI and the MFRSRs, respectively. Both have full width half maximum values of 80 and 10 nm, respectively. In this spectral region, the clear atmosphere and clouds show only small changes in optical properties and minor absorption by ozone [*Alexandrov et al.*, 2002; *Nunez et al.*, 2005]. Thus only minor inconsistencies are expected due to the different spectral response of the channels. In particular, replacing data from the MFRSR's 670 nm channel with data from the 615 nm channel causes negligible changes to our results, due to the very high degree of correlation between both channels. Due to the small absorption optical thickness, the fractions of radiative flux reflected into space and absorbed at the surface will add up to near-unity, and the low land surface albedo leads to a strong contrast between clear-sky and cloudy satellite pixels.

[16] The radiances from both instruments have been converted to atmospheric flux transmittance and bidirectional reflectance by normalization with the in-band normal solar TOA irradiance (using the solar spectrum of *Kurucz* [1995]), the cosine of the solar zenith angle (calculated based on the work of *Michalsky* [1988]), and the square of the ratio of the actual to mean sun-earth distance [*Spencer*, 1971].

3. Method

[17] The 5 minute resolution time series of bidirectional TOA reflectance and atmospheric flux transmittance were subject to a multiresolution analysis (MRA) based on the maximum overlap discrete wavelet transform [*Percival*, 1995] and the Haar wavelet [*Haar*, 1910]. Only a short description of the methodology is given here, while a more formal mathematical treatment and references to the relevant literature are given in the Appendix A.

[18] Figure 1 shows results of the MRA for Cabauw on 23 June 2007, up to a scale $J = 4$. The synoptic situation on this day was determined by an upper-air trough above the British Isles. The trough was slowly moving eastward and advected moist and unstable air to the Netherlands with a westerly airflow. This caused convective activity and frequent showers throughout the Netherlands. Only one shower occurred at Cabauw around at 12 UTC, which is reflected in Figure 1 by low atmospheric transmittance at this time. The bidirectional reflectance and flux transmittance are plotted as red and blue lines, respectively. The top-left panel contains the original time series denoted by S_0. Four smoothed versions S_J, $J \in \{1 \ldots 4\}$ of the original time series, called the wavelet smooths, are shown in the panels below the original. The S_J are obtained as moving averages of $l = 2^J$ samples of the original time series, corresponding to an averaging period of $\Delta t = 5 \times 2^J$ minutes. Thus the maximum averaging period in Figure 1 is 80 minutes and is used to obtain S_4. In the right panels, the wavelet details D_J are shown. At scale J, the wavelet detail D_J is given by the difference between S_{J-1} and S_J. In essence, the wavelet smooth S_J is obtained by low-pass filtering the smooth S_{J-1} with a cutoff frequency of $2^{-(J-0.5)}$, using the rectangular function of length 5×2^J as lowpass filter. The wavelet detail D_J is the difference between filtered and unfiltered time series. The choice of the rectangular function as lowpass filter has been made for two reasons: arithmetic averaging is often applied to meteorological measurements, because it is simpler to interpret than weighted averages. Also, the length of the smoothing window is minimal, and thus the loss of data caused by gaps in the time series due to edge effects. The latter fact is of particular importance for this study, because atmospheric transmittance and reflectance can only be determined for periods with sufficiently high sun elevations. The drawback of the rectangular function is a suboptimal frequency separation [e.g., *Harris*, 1978]. This will result in a somewhat lower explained variance between ground and satellite time series than obtained, e.g., by Gaussian averaging [*Greuell and Roebeling*, 2009].

[19] Two features of the MRA are clearly visible in Figure 1. With increasing scale J, an increasing negative correlation between variations in reflectance and transmittance is visible, as is expected from one-dimensional radiative transfer theory in cloudy atmospheres [see, e.g., *King*, 1987], while the correlation at small timescales is low. The correlation coefficients for the wavelet details range from -0.25 at $J = 1$ to -0.85 at $J = 4$. We also see from Figure 1 that the time series of transmittance exhibits significantly more variability than the bidirectional reflectance, in particular for small scales. Both effects are typical also for other days, and will be investigated more quantitatively in the next section.

4. Results and Discussion

4.1. Effects of Spatial Collocation

[20] An accurate geolocation of SEVIRI images is an important prerequisite for an optimal collocation of the MFRSR and SEVIRI time series. The geostationary satellite projection [*Wolf and Just*, 1999] as implemented by the PROJ.4 cartographic projections library [*Evenden*, 1995] has been used to calculate the satellite viewing angles for the two MFRSR locations and to convert them to SEVIRI pixel indices. We adopt the conventions specified in *Müller et al.* [2007, section 3.1.5], with pixel indices starting from 1 in the southeastern corner of the 3712 × 3712 pixel image. The pixel with indices (1856, 1856) is centered on the nominal subsatellite point at 0° latitude/longitude. For reporting the location of the surface stations within the satellite images in Table 1, fractional pixel indices are used. By convention, a decimal fraction of zero corresponds to the center of each pixel, consistent with the position of the axis tick marks displayed in Figure 2.

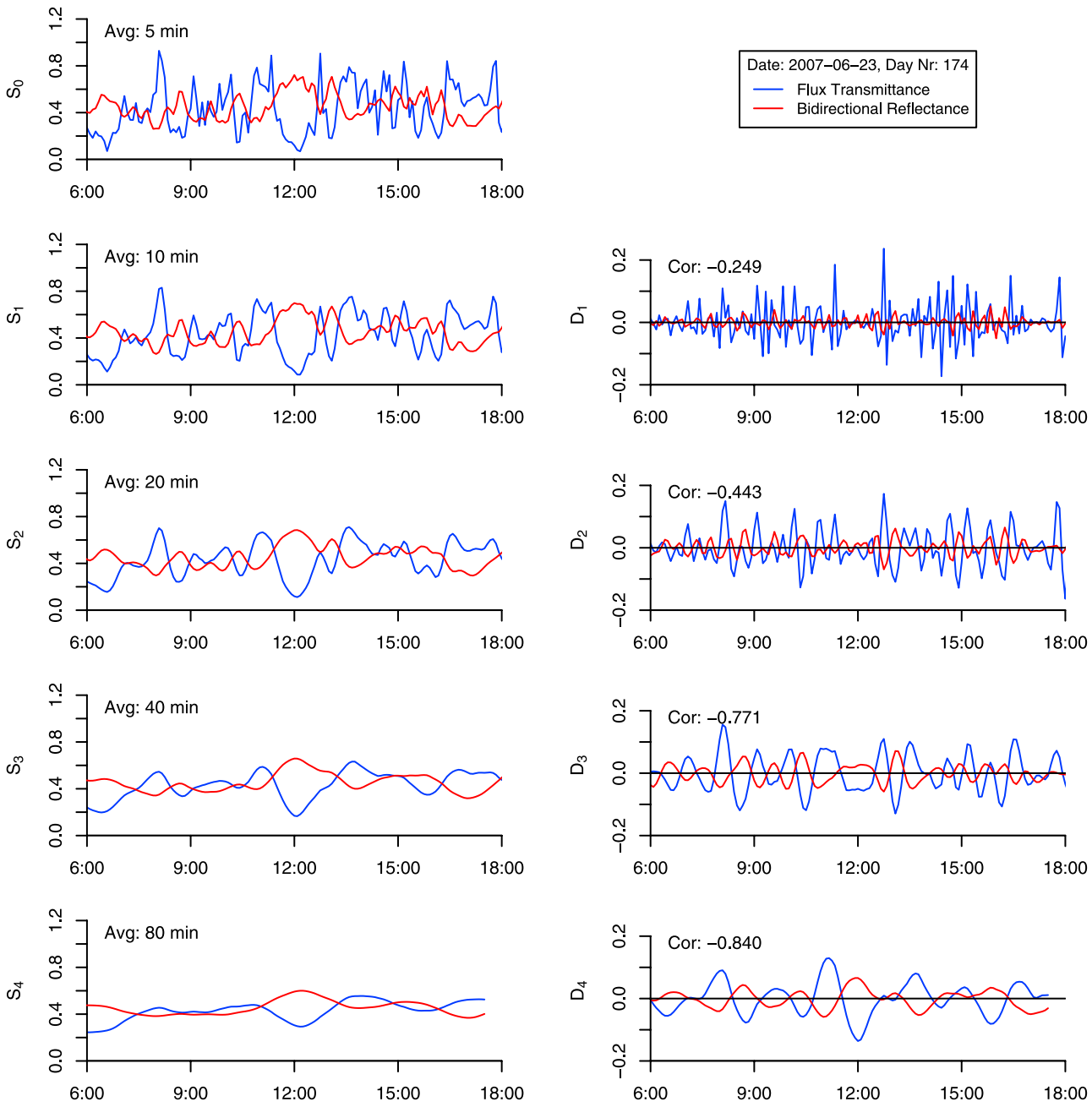

Figure 1. Multiresolution analysis based on the Haar wavelet and the maximum overlap discrete wavelet transform of the time series of atmospheric flux transmittance (blue) and TOA bidirectional reflectance (red) at 0.6 μm. (left) The 5-minute average data (S_0) and the wavelet smooths (S_J) and (right) the wavelet details (D_J) for timescales $J = 5 \times 2^J$ minutes, $J \in \{1 \ldots 4\}$. Data are shown for the daylight hours of 23 June 2007 and for the station Cabauw in the Netherlands. Correlation coefficients of transmittance and reflectance are listed in each panel.

[21] To quantify the effects of spatial collocation, satellite time series have been extracted for a 16 × 16 pixel grid centered around both ground stations. For each of the 256 time series, the explained variance, given by the square of the linear correlation coefficient, has been calculated. This measure is used in the context of regression: if a linear model is used to relate two quantities, the explained variance is the ratio of modeled to total variance for the dependent quantity, and invariant to the choice of dependent variable. Results are shown as contour/intensity plots in Figures 2a and 2b for the two stations. In each panel, the location of the MFRSR is marked by a black cross.

[22] The maxima in explained variance are shifted about 1 pixel to the North of the positions of the ground stations (corresponding to about 6 km). The pixel indices for the maxima are given in Table 1. Considering SEVIRI's specified nominal geolocation accuracy of 0.5 pixels, this displacement is unlikely to be solely caused by a geolocation error. A more plausible explanation is the parallax effect resulting from the large satellite viewing angle of nearly 60°

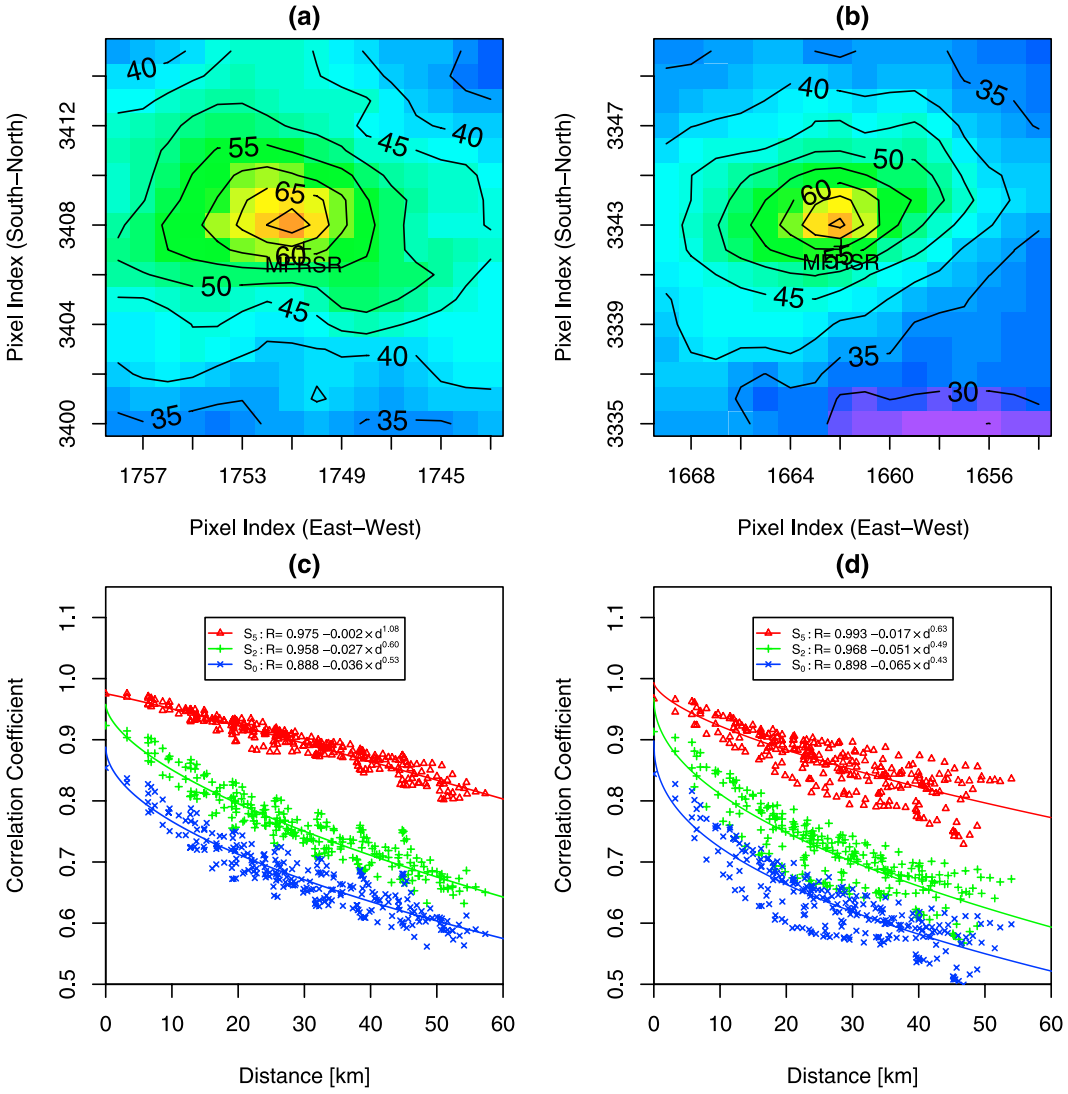

Figure 2. Effects of collocation between satellite and surface measurement. (a, b) Contour/intensity map of explained variance (in %) between the 5-minute resolution time series of surface transmittance and TOA reflectance for a 16 × 16 pixel grid centered around the MFRSRs. (c, d) Absolute values of correlation R of transmittance and reflectance as function of distance d between MFRSR and the pixel center for the original time series S_0, the wavelet smooths S_2 and S_5, and all pixels shown in Figures 2a and 2b. Least square fits of functional form $|R| = a - b \times d^c$ have been added, with fit coefficients given in the legend. Figure 2a, 2c and Figure 2b, 2d have been obtained for the stations of Cabauw and Heselbach, respectively.

for Cabauw and Heselbach, and the height of cloud tops above the earth surface. At this viewing angle, a cloud top height of about 3500 m does explain the observed shift of 1 pixel to the North.

[23] This finding is consistent with the conclusions of *Greuell and Roebeling* [2009] and *Schutgens and Roebeling* [2009]. The former study reports a mean cloud top height of 2600 m for water clouds at Cabauw based on cloud radar observations, and finds a statistically significant increase in correlation between satellite-inferred liquid water path and that obtained from ground-based microwave radiometer measurements when accounting for this shift. Using synthetic high-resolution cloud fields generated based on MODIS data, the latter study identifies the parallax effect as the dominant source of error in a comparison of liquid water path obtained from surface and geostationary satellite data sets over Central Europe. Nevertheless, the limits imposed by the geolocation accuracy and pixel resolution of the SEVIRI instrument do not allow for a definite attribution of the shift of the maxima in explained variance to the parallax effect, and additional confirmation based on surface measurements at different satellite viewing angles seems desirable.

[24] A steep decline in explained variance with increasing distance to the optimal pixel is clearly visible, which highlights the importance of an accurate geolocation. This decline is steeper in the North-South than in the East-West direction, due to the higher effective pixel resolution in the latter direction [see *Müller et al.*, 2007, Figures 9 and 10]. A function of distance d of the form $|R| = a - b \times d^c$ has been fitted to the correlation coefficient R for all 256 pixels

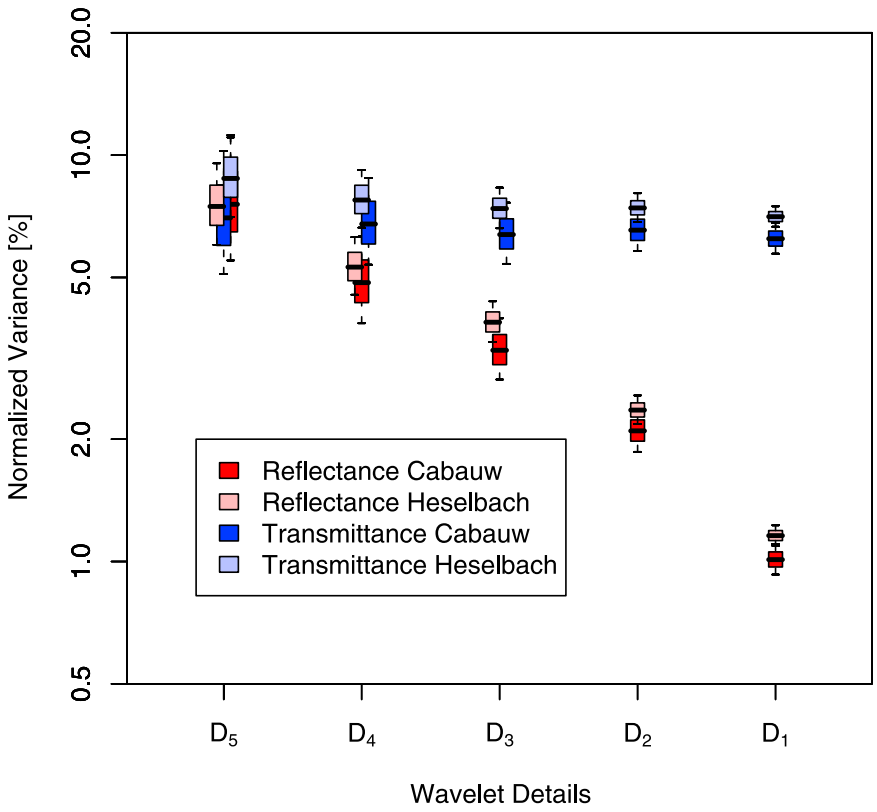

Figure 3. The variance for the wavelet details $D_5, \ldots, D_1$ for the stations of Cabauw and Heselbach, normalized to the total variance of the original time series. The values for the atmospheric flux transmittance as measured by the MFRSR, and the bidirectional reflectance inferred from SEVIRI. The actual value is indicated by the solid black bar, and the colored region and whiskers extend out to delimit the 66% and 95% confidence intervals, respectively.

shown in Figures 2a and 2b. Results are shown for the wavelet smooths S_J, $J \in \{0, 2, 5\}$ in Figures 2c and 2d, and include the fit coefficients in the legend. The fit function extends the linear model used by *Long and Ackerman* [1995] to parameterize the dependence of correlation of atmospheric flux transmittance at separate sites on their distance. Assuming a linear relation between transmittance and reflectance, their model should also be applicable to the situation considered here. However, this seems to be only fulfilled for Cabauw at scale S_5. Otherwise, the correlation falls of faster than linear at small distances, as is indicated by the exponent $c < 1$, in particular for shorter averaging periods and at Heselbach.

[25] The results at the two stations show some differences: the maximal explained variance has a value of 71.2% versus 72.9% for Heselbach and Cabauw, respectively. More noteworthy seems to be the steeper decline of explained variance with distance at Heselbach than at Cabauw, in particular in the southeastern direction. While the period used for this investigation is too short for climatologically significant conclusions, it seems plausible that the variable orography at Heselbach, which results in stronger convective activity, is responsible for this difference. Strong convective activity in fact motivated its choice for the location of the Convective and Orographically Induced Precipitation Study, and might cause more spatial heterogeneity in clouds.

4.2. Scale Dependence of Variance and Correlation

[26] In this section, the effects of the averaging time on the variance of the time series, and on the correlation of atmospheric flux transmittance and bidirectional reflectance, are studied.

[27] Figure 3 shows the scale-dependent variance of the wavelet details D_J, $J \in \{1 \ldots 5\}$ for reflectance and transmittance at Cabauw and Heselbach, normalized to the total variance of the full 5 minute resolution time series. This normalization has been chosen to ensure better comparability between the values for transmittance and reflectance, by removing the effects of a nonunity slope in an assumed linear relation between both quantities. Both time series exhibit a very different scaling behavior: for the reflectance, a linear decrease of variance with increasing frequency is found. In contrast, the variance of the transmittance remains nearly constant across the considered frequency range. As a result, the wavelet details contribute nearly 40% of the total variance for the transmittance, versus only about 20% for the reflectance, indicating significantly larger high-frequency variability of the transmittance.

[28] The difference in the wavelet variance spectra of transmittance and reflectance at high temporal frequencies implies that any attempt to explain both measurements simultaneously based on one-dimensional radiative transfer theory must fail: without horizontal photon transport and in the absence of absorption, photons have to leave an implicitly

assumed atmospheric column either through the upper or lower boundary. This will cause perfect correlation between variations in flux through both boundaries. The effects of the minor amounts of atmospheric absorption at 0.6 m and the use of bidirectional reflectance instead of TOA albedo in this study are too small to fully explain the lack of correlation at high temporal frequencies.

[29] *Barker and Li* [1997] show that due to their point nature, solar surface irradiance measurements introduce significant sampling uncertainties for estimating the surface flux corresponding to the 6 × 3 km pixel size of SEVIRI. This suggests that significant spatial variability affects surface irradiance measurements, despite the hemispheric field of view of the instruments. This hypothesis is also supported by the study of *Boers et al.* [2000], which demonstrates that the solar surface irradiance is very sensitive to cloud inhomogeneities, in particular for broken cloud fields due to the contributions from the direct irradiance.

[30] If sampling uncertainties were the only reason for the observed effects, an increased resolution of the satellite sensor should significantly modify the wavelet spectrum of reflectance, and reduce the difference between the reflectance and transmittance spectra. *Barker and Li* [1997] however also report increasing deviations from one-dimensional radiative transfer due to horizontal photon transport, if the horizontal dimensions of an atmospheric column under consideration are decreased. Further evidence for the relevance of three-dimensional radiative transfer effects is given by *Horvath and Davies* [2004], who find that the anisotropy of reflected solar radiation increasingly deviates from one-dimensional radiative transfer calculations, if the spatial resolution of a satellite is increased, and by *Kassianov et al.* [2005], who show that the atmospheric transmittance and reflectance have different sensitivities to spatial resolution in cloudy conditions. Full three-dimensional radiative transfer calculations based on realistic cloud fields could clarify the relevance of the individual effects mentioned here.

[31] As a consequence of the different scaling properties, reflectances observed by SEVIRI cannot be used to obtain a data set of atmospheric transmittance with high temporal resolution and realistic variability at high frequencies. For applications imposing such requirements, one option would be to add synthetic high-frequency variations with realistic scaling properties (see, e.g., *Venema et al.* [2006], for a discussion of suitable methods).

[32] Figure 3 shows that the variance of the satellite reflectance falls off approximately linearly with increasing frequency on a log-log scale. At a period of 10 minutes, the variance contributes less than 2% to the total variance. This suggests that a further decrease of the satellite repeat cycle to less than 5 minutes would likely cause only a minor increase in total variance. This finding is advantageous for our study, as the reflectance time series consists not of 5 minute averages, but of instantaneous samples. Sampled time series are potentially susceptible to the aliasing effect: if significant variability is present in a signal at high frequencies beyond the Nyquist frequency, which is given by half the sampling frequency, it becomes indistinguishable after sampling from the variability at lower frequencies. As only a small amount of variance is expected beyond the Nyquist frequency by extrapolation of the variance spectrum, the aliasing effect should have only a minor influence on our analysis.

[33] Figure 4 presents the fraction of explained variance of transmittance and reflectance for the wavelet smooth S_5 and the wavelet details D_J, $J \in \{1 \ldots 5\}$. For S_5, i.e. an averaging time of 160 minutes, values of 95.0 and 93.5% are found at Cabauw and Heselbach, respectively, indicating an excellent degree of correlation. For the wavelet details, the explained variance drops from about 60% at D_5 to 3% at D_1. For variations with a period of less than an hour, the explained variance lies significantly below 50%, which shows that random fluctuations start to dominate over the connection implied in one-dimensional radiative transfer theory. While not statistically significant at the 95% confidence level, values of explained variance for the wavelet details are higher at Heselbach than at Cabauw at all scales. Again, a possible explanation might be found in the stronger convective activity and the resulting differences in cloud properties at the Heselbach site.

4.3. Implications for Validation of Satellite Products

[34] The results of this study have important implications for the validation of satellite products of solar surface irradiance by a comparison to ground measurements, as the situation discussed here is very similar to such a comparison, as pointed out by *Nunez et al.* [2005]. Comparable effects also have to be expected for the validation of cloud products retrieved from passive satellite imagers such as cloud water path by comparison to surface observations. The quality of a retrieval is usually quantified by metrics such as the explained variance or the root mean square error, and suitable averaging periods are often determined by studying the sensitivity of these metrics to the averaging period [e.g., *Deneke et al.*, 2005].

[35] Figure 5 illustrates this approach. It displays contour/intensity plots of explained variance as function of smoothing scale J for both the satellite and surface time series. If the wavelet spectra of transmittance and reflectance contained identical variance at all scales, the plot would have to be symmetrical along the diagonal (indicated by the dashed line). The asymmetry can thus be attributed to differences in the scaling properties discussed already. Two independent effects pointed out in section 4.2 influence the behavior of the explained variance, which can no longer be distinguished in Figure 5: first, variance is removed at high frequencies by increasing the averaging period. This loss of information increases with the length of averaging period. Second, correlation is strongly scale-dependent and increases with decreasing frequency of variations. The choice of the averaging period for a comparison of both quantities is thus a tradeoff between preserving the variance of the original data set and limiting the comparison to coupled scales of variance. If the quality of retrievals is compared after selection of a suitable averaging period using the correlation as metric (or explained variance, which is the square of correlation), it needs to be recognized that the correlation is a weighted average of the scale-dependent correlations, with the variance spectra of the time series determining the weighting. Thus changes in the variance spectra of transmittance and reflectance, e.g., caused by different cloud climatologies at different sites, can alter the values of correlation, and could possibly even change a quality ranking of retrievals.

[36] Two different validation situations are discussed in more detail in the following: instantaneous estimates

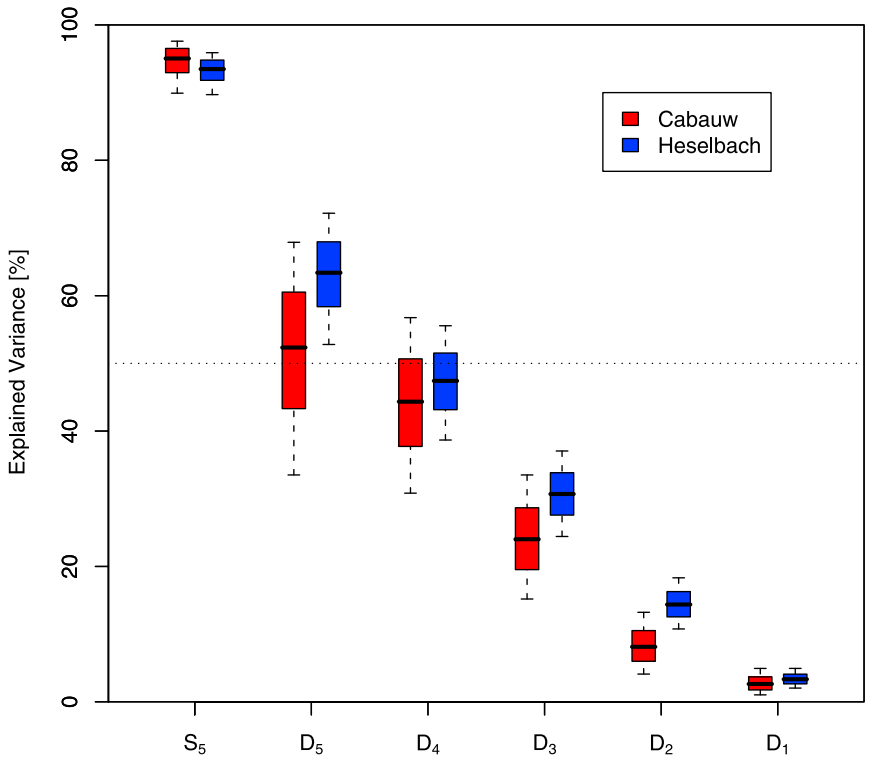

Figure 4. Explained variance (in %) for the wavelet smooth S_5 and the wavelet details $D_5, \ldots, D_1$ of the time series of atmospheric flux transmittance and bidirectional reflectance for the stations of Cabauw (red) and Heselbach (blue). The actual value of explained variance is indicated by the solid black bar, and the colored region and whiskers delimit the 66% and 95% confidence intervals, respectively.

as obtained from polar-orbiting satellites, and time series obtained from geostationary instruments such as METEOSAT SEVIRI.

[37] For instantaneous products derived from satellite images, the choice of the averaging period can be represented by a cross section parallel to the ordinate through the abscissa value of $J = 0$ in Figure 5, which has been marked by the dotted lines. The maximal explained variance is found for a smoothing scale J between 3 and 4, corresponding to 40–80 minutes. Thus using an averaging period in that range, all scales containing significantly more variance in transmittance than in reflectance are removed prior to the comparison, as can be verified in Figure 3. A further increase of the averaging period will also remove low-frequency variations in transmittance which are well resolved by the reflectance measurement, and will thus reduce the agreement between satellite and surface time series. These findings provide an a posteriori justification for the choice of a 40 minute averaging period for the validation of AVHRR-based estimates of surface solar irradiance with ground measurements by *Deneke et al.* [2005].

[38] For geostationary satellite imagers, the averaging period used for the satellite time series provides an additional degree of freedom. It is advisable to choose identical averaging periods for satellite- and ground-based time series, as both observations are modulated by the same physical processes. As in the case of instantaneous images, the comparison should be restricted to timescales with both significant correlation and similar variance, which imposes a lower limit of 40 minutes for the averaging period again. *Deneke et al.* [2008] therefore compared hourly averages of solar irradiance measured at the surface and inferred from SEVIRI. Longer averaging periods will increase the explained variance, as long as the correlation between variations in reflectance and transmittance also increases with period. This is confirmed by the maxima found in the upper left corners of both panels in Figure 5. In contrast to the case of instantaneous images, no upper limit on explained variance is found, as low-frequency variations are now removed from both the satellite and surface time series. As mentioned before, the increase of averaging period also causes a decrease of variance, however, and thus a loss of information by removal of small-scale variability. Whether this loss is acceptable depends on the requirements of specific applications. It should also be noted that temporal averaging of the satellite time series will generally improve the validation statistics. This implies that validation results for geostationary imagers using temporal averaging cannot be fairly compared to those obtained for polar-orbiting imagers, which are only able to provide instantaneous estimates. Aliasing effects due to a too low satellite scan frequency can cause additional complications, which are neglected here, as they have been shown to be small for our investigation.

[39] An interesting aspect is also the regional differences found between the Heselbach and Cabauw sites. Both the wavelet variance spectra and the scale-dependent correlation are different, with Heselbach having both higher variance and correlation at timescales below an hour. As explanation, we propose the stronger convective activity at Heselbach due to orography, which will likely modify cloud structure and the

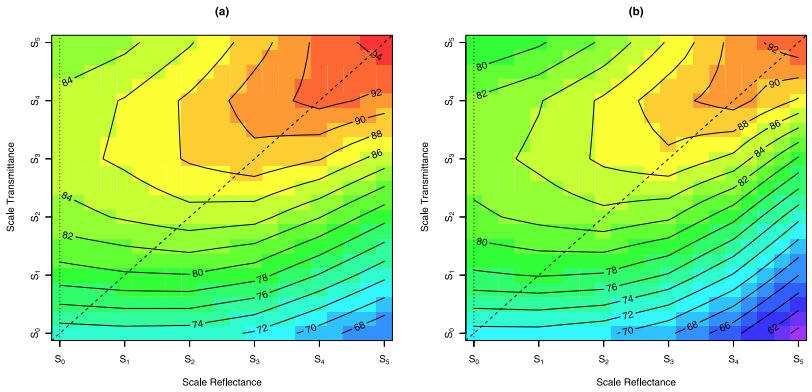

Figure 5. Explained variance (in %) for the wavelet smooths S_0, ..., S_5 of atmospheric flux transmittance and bidirectional reflectance at (a) Cabauw and (b) Heselbach. The resolution of the data field has been increased by a factor of 4 using bilinear interpolation. The dotted and dashed lines have been added to aid the discussion in the text.

frequency of cloud types. Convective clouds are known to have a strong impact on the temporal variability of the solar surface irradiance [*Duchon and O'Malley*, 1999]. While the comparison period is too short for climatologically meaningful results, it demonstrates that validation statistics obtained at a single station or for a specific region might not be representative for other regions. This also implies that the recommendations given here for an optimal averaging period might not necessarily hold for other geographic locations or seasons.

[40] Finally, we want to point out the main limitations of our approach for studying the comparison of satellite retrievals of solar surface irradiance and surface measurements: a linear relation between transmittance and reflectance is assumed, and only a narrow spectral region has been considered. A particular retrieval scheme of solar surface irradiance might also incorporate nonlinear effects and considers radiative transfer for the complete solar spectral range. While these factors should not change our conclusions qualitatively, some quantitative differences can be expected.

5. Conclusions and Outlook

[41] Collocated time series of 0.6 μm narrowband bidirectional reflectance and flux transmittance measured by METEOSAT SEVIRI in rapid scan mode, and 2 multifilter rotating shadowband radiometers operated at Cabauw, the Netherlands, and Heselbach, Germany, have been compared in this study. A wavelet-based multiresolution analysis has been used to determine the temporal scaling properties of both time series and their timescale-dependent correlation.

[42] Our results support that the parallax effect, an apparent shift in geolocation due to the altitude of cloud tops and oblique satellite viewing geometries needs to be corrected for to obtain optimum agreement between satellite and surface time series for larger satellite viewing angles.

[43] Reflectance and transmittance have been found to be highly anticorrelated for temporal variations with a period of an hour or longer, whereas this correlation breaks down for shorter periods. Significantly larger variance in transmittance than in reflectance has been observed for small timescales. Hence a consistent interpretation of both time series based on plane-parallel horizontally homogeneous clouds and one-dimensional radiative transfer is no longer possible for variations with periods below an hour. Likely reasons for this phenomenon are horizontal photon transport and the different spatial averaging scales of the satellite and ground measurements [*Barker and Li*, 1997; *Kassianov et al.*, 2005].

[44] Based on these observations, we have discussed the selection of suitable averaging periods for the validation of satellite retrievals of solar surface irradiance with ground-based measurements. For instantaneous estimates such as those obtained from polar-orbiting satellites, an averaging period in the order of 40 to 80 minutes will ensure an optimum agreement with ground-based measurements for our data set. For time series inferred from geostationary satellites, the use of identical averaging periods is recommended, which should also not be chosen below 40 minutes.

[45] Additional confirmation should be sought before adopting these recommendations to other climate regions or satellite sensors, as the effects discussed in this study depend on cloud type, and possibly on sensor resolution. This is supported by the differences in variability observed between the Cabauw and Heselbach sites. These differences are not significant in a strict statistical sense, but this is likely due to the short period used for this comparison.

[46] This study demonstrates that the multiresolution analysis is well suited to investigate the scaling properties of time series and the scale-dependent correlation of related quantities. We have successfully applied it to quantify the influence of temporal averaging period on retrieval quality and validation statistics. The multiresolution analysis could be utilized in a similar manner to study the effects of spatial averaging. Other applications in the field of remote sensing also seem promising, such as the selection of suitable averaging scales for the synergetic use of multisensor data sets.

[47] Several extensions of this study could lead to additional scientific insights: SEVIRI's high resolution visible channel with a spatial resolution of 1×1 km^2 should allow a more accurate estimate of the parallax effect, and could be used to determine the influence of satellite resolution on the wavelet variance spectrum for the reflectance. In this study, only radiative quantities have been considered. However, a

number of cloud properties are operationally retrieved from METEOSAT SEVIRI [*Schulz et al.*, 2008]. In particular, the methodology presented here could be applied to the validation of liquid water path with ground-based microwave radiometer measurements [*Roebeling et al.*, 2008], and could thus be used to investigate the link between cloud structure and radiation. As radiation is strongly modulated by cloud properties, this link is of high importance for our understanding of the climate system.

Appendix A: Multiresolution Analysis and Wavelets

[48] This appendix presents a brief summary of the multiresolution analysis and its relation to the discrete wavelet transform. In addition, the concepts of the scale-dependent wavelet variance and correlation are introduced, including confidence intervals to assess their statistical uncertainties.

[49] For more detailed treatments of the subject, the reader is referred to standard text books [e.g., *Mallat*, 1998] and the quoted references.

[50] The Hilbert space $L^2(R)$ of square-integrable functions of a single variable (the time t here) with scalar product $\langle f|g\rangle \equiv \int_R f(t)\,\overline{g(t)}\,dt$ is considered here. A multiresolution analysis [MRA, *Mallat*, 1989] of the space $L^2(R)$ is defined as sequence of nested subspaces $\{V_m\}$, $m \in Z$, which fulfill the following conditions:

$$\{0\} \subset \ldots \subset V_1 \subset V_0 \subset V_{-1} \subset \ldots \subset L^2(R), \tag{A1}$$

$$\bigcup_{m\in Z} V_m = L^2(R),\ \bigcap_{m\in Z} V_m = \{0\}, \tag{A2}$$

$$f(t) \in V_m \Longleftrightarrow f(2t) \in V_{m+1}, \tag{A3}$$

$$f(t) \in V_0 \Longrightarrow f(t-k) \in V_0\ \forall k \in Z, \tag{A4}$$

$$\exists\ \varphi(t):\ \{\varphi(t-k),\ k \in Z\} \text{ is orthonormal basis of } V_0. \tag{A5}$$

Equations (A1) and (A2) imply that starting with the zero function, the V_m can support functions with increasing level of detail for decreasing m, and span the complete $L^2(R)$ for $m \to -\infty$. Equations (A3) and (A4) describe the behavior under scaling and translation, while equation (A5) requires the existence of a basis φ for V_0, which is called the scaling function of the MRA. The spaces W_n are now defined as the orthogonal complements of V_n in V_{n-1}, or less formally, to contain those variations of a function in V_{n-1} which do not fit into V_n. For a scaling function φ of an MRA, there exists an associated function ψ, which forms an orthonormal basis of the space W_0, and is a wavelet. Scaled and translated versions of the scaling and wavelet function are orthonormal bases of V_m and W_m:

$$\varphi_{m,k} \equiv 2^{-m/2}\ \varphi(2^{-m}x-k),\ \psi_{m,k} \equiv 2^{-m/2}\ \psi(2^{-m}x-k). \tag{A6}$$

[51] We now consider the expansion coefficients $v_k^m \equiv \langle f|\varphi_{m,k}\rangle$, $w_k^m \equiv \langle f|\psi_{m,k}\rangle$ of a function f on these bases, and require that a function $f(t)$ is contained in V_0 for a specific MRA. It follows that $w_k^m = 0$ for all $m \le 0$. f can be decomposed into a smooth signal in V_J, and the variations contained in W_m, $m \in [1 \ldots J]$:

$$f(t) = \underbrace{\sum_{k\in Z} v_k^0\,\varphi_{0,k}}_{\in V_0} = \underbrace{\sum_{k\in Z} v_k^J\,\varphi_{J,k}}_{\in V_J} + \sum_{m=1}^{J} \underbrace{\sum_{k\in Z} w_k^m\,\psi_{j,k}}_{\in W_j}. \tag{A7}$$

The wavelet smooths $S_m \equiv \sum_{k\in Z} v_k^m\ \varphi_{m,k}$ and wavelet details $D_m \equiv \sum_{k\in Z} w_k^m\ \psi_{m,k}$ of the function f are its projection on the spaces V_J and W_J, respectively. The set of coefficients $\{v_k^J\}$ and $\{w_k^j\}$, $j \in \{1 \ldots J\}$ constitute the discrete wavelet transform (DWT) of the function f, and can be efficiently calculated for any scale J given the $\{v_k^0\}$, plus characteristic filter coefficients for a specific wavelet and scaling function having compact support [*Mallat*, 1989]. These filter coefficients characterize the frequency response of the scaling and wavelet functions considered as finite impulse response filters.

[52] The DWT forms an orthonormal and thus nonredundant representation of the function f. The maximum-overlap or nondecimated discrete wavelet transform (MODWT) is a variant of the DWT, which uses the expansion coefficients $\tilde{v}_k^m \equiv \langle f|\tilde{\varphi}_{m,k}\rangle$ and $\tilde{w}_k^m \equiv \langle f|\tilde{\psi}_{m,k}\rangle$, with

$$\tilde{\varphi}_{m,k} \equiv 2^{-m}\ \varphi(2^{-m}(x-k)),\ \tilde{\psi}_{m,k} \equiv 2^{-m}\ \psi(2^{-m}(x-k)). \tag{A8}$$

Thereby, the orthonormality is given up, as now a function having N nonzero coefficients v_k^0 is represented by $N \times J$ MODWT coefficients for an MRA up to scale J instead of only N coefficients for the DWT. Wavelet smooths and details are defined analogous to the DWT, with $\tilde{S}_m \equiv \sum_{k\in Z} \tilde{v}_k^m\ \tilde{\varphi}_{m,k}$ and $\tilde{D}_m \equiv \sum_{k\in Z} \tilde{w}_k^m\ \tilde{\psi}_{m,k}$. There are several advantages over the DWT [*Percival*, 1995]. Most important for our application, the number of samples does not need to be an integer power of 2, and events at specific times can be aligned in the original time series and the wavelet smooths and details. Also, the MODWT coefficients are more accurate for estimating the variance at specific timescales than the DWT coefficients. An efficient pyramid algorithm for calculating the MODWT coefficients using the filtering coefficients of the scaling and wavelet function is given by *Percival* [1995].

[53] In this paper, the Haar wavelet [*Haar*, 1910] is used for the MRA. Its corresponding scaling function is the rectangular function, and scaling and wavelet functions are shown in Figure A1. Also, their amplitude responses, given by the modulus of the Fourier transform, are shown. The scaling and wavelet functions act as a lowpass and bandpass filters, respectively, as they let through frequencies in the normalized frequency range mainly below 0.5, and between 0.5 and 1. The Haar MRA has been chosen for our study, as it has maximum time localization, thereby minimizing the support of the filters, as well as the range of edge effects. This is of particular importance in our case, as the length of our time series is limited due the fact that atmo-

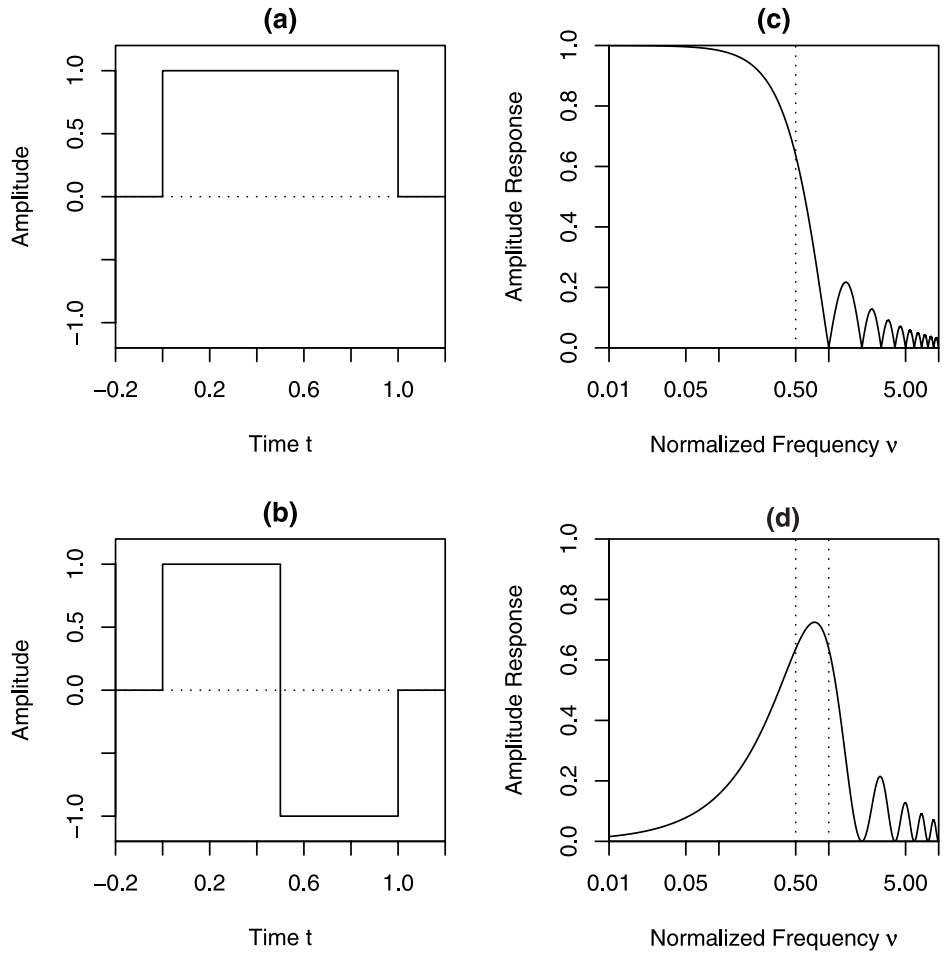

Figure A1. Time representation of the Haar (a) scaling and (b) wavelet function, and the frequency response of the associated (c) lowpass and (d) bandpass filters.

spheric transmittance and reflectance can only be determined accurately at sufficiently high sun elevations. As a drawback of this choice, the filter characteristics allow only a fairly bad frequency separation [*Harris*, 1978].

[54] *Percival* [1995] shows that the MODWT decomposes the variance of a time series f on a scale-by-scale basis, and can be estimated from the variance of the MODWT coefficients:

$$\|f\|^2 = \|v_J\|^2 + \sum_{j=1}^{J} \|w_j\|^2. \tag{A9}$$

Based on equations (6) and (9) of *Percival* [1995], approximate confidence intervals can be constructed for the true scale-dependent wavelet variance ν_J^2, given the estimate $\tilde{\nu}_J^2$ obtained from the MODWT coefficients:

$$\nu_J^2 \in \left[\frac{N\,\tilde{\nu}_J^2}{2^J\,\Psi(1-p,\eta)}, \frac{N\,\tilde{\nu}_J^2}{2^J\,\Psi(p,\eta)}\right]. \tag{A10}$$

Whitcher et al. [2000] extend this result by showing that the correlation of the wavelet coefficients of two time series provides an estimate of the correlation of the two time series at a given scale. For the wavelet correlation, confidence intervals are given by:

$$\gamma_J \in \left[\tanh\left(\operatorname{atanh}^{-1}(\tilde{\gamma}) - \frac{\Phi^{-1}(1-p)}{\sqrt{\frac{N}{2^J}-3}}\right), \tanh\left(\operatorname{atanh}^{-1}(\tilde{\gamma}) + \frac{\Phi^{-1}(1-p)}{\sqrt{\frac{N}{2^J}-3}}\right)\right]. \tag{A11}$$

In both equations, p is the desired single-sided confidence level, N is the remaining number of wavelet coefficients after removal of coefficients with edge contributions, Ψ and Φ are the quantile functions of the χ^2 and normal random number distributions, respectively, and J is the wavelet scale under consideration. These confidence intervals assume that the degree of freedom of the MODWT coefficients decreases with scale as 2^J, but are otherwise uncorrelated (see *McCoy and Walden* [1996], for a discussion of this assumption). Thus longer-term autocorrelation, e.g., caused by the prevalence of specific synoptic weather conditions during our study, are not accounted for.

[55] **Acknowledgments.** The first author's work was funded by a EUMETSAT research fellowship. The authors are grateful to the ARM project for providing MFRSR data from the ARM mobile facility in Heselbach, Germany. The use of the R Language for statistical computing [*R Development Core Team*, 2007] and in particular the waveslim package [*Whitcher*, 2007] are acknowledged. We also thank our colleagues Wouter Greuell, Rob Roebeling, Victor Venema, and Erwin Wolters, as well as the three anonymous reviewers, for their helpful suggestions and comments, which significantly improved the final version of this manuscript.

References

Alexandrov, M., A. Lacis, B. Carlson, and B. Cairns (2002), Remote sensing of atmospheric aerosols and trace gases by means of multifilter rotating shadowband radiometer. Part I: Retrieval algorithm, *J. Atmos. Sci.*, *59*, 524–543.

Barker, H., and Z. Li (1997), Interpreting shortwave albedo-transmittance plots: True or apparent anomalous absorption?, *Geophys. Res. Lett.*, *24*(16), 2023–2027.

Boers, R., A. van Lammeren, and A. Feijt (2000), Accuracy of cloud optical depth retrievals from ground based pyranometers, *J. Atmos. Ocean Technol.*, *17*, 916–927.

Deneke, H., A. Feijt, A. Lammeren, and C. Simmer (2005), Validation of a physical retrieval scheme of solar surface irradiances from narrowband satellite radiances., *J. Appl. Meteorol.*, *44*(9), 1453–1466.

Deneke, H., A. Feijt, and R. Roebeling (2008), Estimating surface solar irradiance from METEOSAT SEVIRI-derived cloud properties, *Remote Sens. Environ.*, *112*, 3131–3141.

Duchon, C., and M. O'Malley (1999), Estimating cloud type from pyranometer observations, *J. Appl. Meteorol.*, *38*, 132–141.

Evenden, G. (1995), Cartographic projection procedures for the UNIX environment: A user's manual, *U.S. Geol. Surv. Open-File Rep., 90-284*, U.S. Geol. Surv., Woods Hole, Mass. (Available at http://pubs.usgs.gov/of/of90-284)

Feijt, A., and H. Jonker (2000), Comparison of scaling parameters from spatial and temporal distributions of cloud properties, *J. Geophys. Res.*, *105*(D12), 29,089–29,097.

Greuell, W., and R. Roebeling (2009), Toward a standard procedure for validation of satellite-derived cloud liquid water path, *J. Appl. Meteorol. Climatol.*, doi:10.1175/2009JAMC2112.1, in press.

Haar, A. (1910), Zur theorie der orthogonalen funktionensysteme, *Math. Ann.*, *69*, 331–371.

Harris, F. (1978), On the use of windows for harmonic analysis with the discrete Fourier transform, *Proc. IEEE*, *66*(1), 51–83.

Harrison, L., J. Michalsky, and J. Berndt (1994), Automated multifilter rotating shadow-band radiometer: An instrument for optical depth and radiation measurements, *Appl. Optics*, *33*(22), 5118–5125.

Horvath, A., and R. Davies (2004), Anisotropy of water cloud reflectance: A comparison of measurements and 1D theory, *Geophys. Res. Lett.*, *31*, L01102, doi:10.1029/2003GL018386.

Intergovernmental Panel on Climate Change (2007), *Climate Change 2007: The Physical Science Basis. Contribution of Working Group I to the Fourth Assessment Report of the Intergovernmental Panel on Climate Change*, edited by S. Solomon et al., 18 pp., Cambridge Univ. Press, Cambridge, U. K.

Kassianov, E., T. Ackerman, and P. Kollias (2005), The role of cloud-scale resolution on radiative properties of oceanic cumulus clouds, *J. Quant. Spectrosc. Radiat. Transfer*, *91*, 211–226.

Kiehl, J. T., and K. E. Trenberth (1997), Earth's annual global mean energy budget, *Bull. Am. Meteorol. Soc.*, *78*(2), 197.

King, M. (1987), Determination of the scaled optical thickness of clouds from reflected solar radiation measurements, *J. Atmos. Sci.*, *44*, 1734–1751.

Knap, W., J. Bijma, Y. Hinssen, A. Los, C. van Oort, J. Warmer, and E. Worrell (2007), The Baseline Surface Radiation Network (BSRN) station at the Cabauw Observatory, *KNMI Biennial Scientific Rep.*, chap., pp. 18–23, Royal Netherlands Meteorol. Inst., De Bilt, Netherlands.

Kurucz, R. L. (1995), The solar irradiance by computation, in *Proceedings of the 17th Annual Conference on Atmospheric Transmission Models*, edited by G. P. Anderson et al., pp. 333–334, PL-TR-95-2060, Phillips Lab., Hanscom AFB, Mass. (Available at http://handle.dtic.mil/100.2/ADA295597)

Long, C., and T. Ackerman (1995), Surface mesurements of solar irradiance: A study of the spatial correlation between simultaneous measurements at separate sites, *J. Appl. Meteorol.*, *34*, 1039–1046.

Mallat, S. (1989), A theory for multiresolution signal decomposition: The wavelet representation, *IEEE Trans. Pattern Anal. Mach. Intell.*, *11*(7), 674–693.

Mallat, S. (1998), *A Wavelet Tour to Signal Processing*, 637 pp., Academic, New York.

McCoy, E., and A. Walden (1996), Wavelet analysis and synthesis of stationary long-memory processes, *J. Comput. Graphical Stat.*, *5*(1), 25–56.

Michalsky, J. (1988), The astronomical Almanac's algorithm for approximate solar position (1950–2050), *Solar Energy*, *40*, 227–235.

Müller, J., G. Fowler, K. Dammann, C. Rogers, Y. Buhler, and J. Flewin (2007), MSG level 1.5 image data format description, *EUM/MSG/ICD/105*, EUMETSAT, Darmstadt, Germany.

Nunez, M., K. Fienberg, and C. Kuchinke (2005), Temporal structure of the solar radiation field in cloudy conditions: Are retrievals of hourly averages from space possible?, *J. Appl. Meteorol.*, *44*, 167–178.

Percival, D. (1995), On estimation of the wavelet variance, *Biometrika*, *82*, 619–631.

R Development Core Team (2007), *R: A Language and Environment for Statistical Computing*, R Found. for Stat. Comput., Vienna, Austria. (Available at http://www.r-project.org)

Roebeling, R., H. Deneke, and A. Feijt (2008), Validation of cloud liquid water path retrievals from SEVIRI using one year of CloudNET observations, *J. Appl. Meteorol. Climatol.*, *47*(1), 206–222.

Rossow, W., C. Delo, and B. Cairns (2002), Implications of the observed mesoscale variations of clouds for the Earth's radiation budget, *J. Clim.*, *15*, 557–585.

Schulz, J., et al. (2008), Operational climate monitoring from space: The eumetsat satellite application facility on climate monitoring (CM-SAF), *Atmos. Chem. Phys. Discuss.*, *8*(3), 8517–8563.

Schutgens, N., and R. Roebeling (2009), Validating the validation: The influence of liquid water distribution in clouds on the intercomparison of satellite and surface observations, *J. Atmos. Ocean Technol.*, doi:10.1175/2009JTECHA1226.1, in press.

Spencer, J. W. (1971), Fourier series representation of the position of the sun, *J. Clim.*, *6*, 1764–1772.

Stephens, G. L., and C. D. Kummerow (2007), The remote sensing of clouds and precipitation from space: A review, *J. Atmos. Sci.*, *64*, 3742–3765.

Venema, V., S. Bachner, H. Rust, and C. Simmer (2006), Statistical characteristics of surrogate data based on geophysical measurements, *Nonlinear Processes Geophys.*, *13*, 449–466.

Whitcher, B. (2007), Waveslim: Basic wavelet routines for one-, two- and three-dimensional signal processing, *R Package Version 1.6.1*. (Available at http://r-forge.r-project.org/scm/?group-id=369)

Whitcher, B., P. Guttorp, and D. Percival (2000), Wavelet analysis of covariance with application to atmospheric time series, *J. Geophys. Res.*, *105*(D11), 14,941–14,962.

Wolf, R., and D. Just (1999), LRIT/HRIT Global Specification, *CGMS 03*, EUMETSAT, Darmstadt, Germany.

Wulfmeyer, V., et al. (2008), The convective and orographically-induced precipitation study: A research and development project of the world weather research program for improving quantitative precipitation forecasting in low-mountain regions, *Bull. Am. Meteorol. Soc.*, *89*, 1477–1486, doi:10.1175/2008BAMS2367.1.

H. M. Deneke and W. H. Knap, Department of Climate Research and Seismology, Royal Netherlands Meteorological Institute, Postbus 201, NL-3730 AE De Bilt, Netherlands. (hartwig.deneke@gmail.com)

C. Simmer, Meteorological Institute, University of Bonn, Auf dem Huegel 20, D-53121 Bonn, Germany.